



Royal Netherlands Institute for Sea Research

This is a postprint of:

Romero, O.E., Crosta, X., Kim, J.-H., Pichevin, L. & Crespin, J. (2015). Rapid longitudinal migrations of the filament front off Namibia (SE Atlantic) during the past 70 kyr. *Global and Planetary Change*, 125

Published version: [dx.doi.org/10.1016/j.gloplacha.2014.12.001](https://doi.org/10.1016/j.gloplacha.2014.12.001)

Link NIOZ Repository: www.vliz.be/nl/imis?module=ref&refid=243727

[Article begins on next page]

The NIOZ Repository gives free access to the digital collection of the work of the Royal Netherlands Institute for Sea Research. This archive is managed according to the principles of the [Open Access Movement](#), and the [Open Archive Initiative](#). Each publication should be cited to its original source - please use the reference as presented.

When using parts of, or whole publications in your own work, permission from the author(s) or copyright holder(s) is always needed.

1 Rapid longitudinal migrations of the filament front
2 off Namibia (SE Atlantic) during the past 70 kyr

3

4 O.E. Romero^{1,*}, X. Crosta², J.-H. Kim³, L. Pichevin⁴ and J. Crespin²

5

6 ⁽¹⁾ MARUM - Center for Marine Environmental Sciences, University of Bremen, Leobener Str., 28359 Bremen,
7 Germany. oromero@uni-bremen.de

8 ⁽²⁾ CNRS/INSU, UMR5805, EPOC, Université Bordeaux 1, Talence Cedex, France.

9 ⁽³⁾ NIOZ Royal Netherlands Institute for Sea Research, NL-1790 AB Den Burg, the Netherlands.

10 ⁽⁴⁾ School of Geosciences, Grant Institute, University of Edinburgh, West Main Road, EH10 3JW, Edinburgh,
11 UK.

12 * Corresponding author

13

14

15 Abstract

16 Although productivity variations in coastal upwelling areas are mostly attributed to
17 changes in wind strength, productivity dynamics in the Benguela Upwelling System (BUS) is
18 less straightforward due to its complex atmospheric and hydrographic settings. In view of
19 these settings, past productivity variations in the BUS can be better investigated with
20 downcore sediments representing different productivity regimes. In this study, two sediment
21 cores retrieved at ca. 25°-26°S in the BUS and representing different productivity regimes
22 were studied. By using micropaleontological, geochemical and temperature proxies measured
23 on core MD96-2098, recovered at 2,910 m water depth in the bathypelagic zone at 26°S off
24 Namibia, variations of filament front location, productivity and temperature in the central
25 BUS over the past 70 kyr were reconstructed. The comparison with newly-generated
26 alkenone-based sea-surface temperature (SST) and previously obtained data at site
27 GeoB3606-1 (~25°S; ca. 50 km shoreward from MD96-2098) allowed the recognition of four
28 main phases: (1) upwelling front above the mid slope (70 kyr – 44 kyr), (2) seaward
29 displacement of the upwelling front beyond the mid slope (44 kyr – 31 kyr), (3) main
30 upwelling front over the hemipelagial (31 kyr – 19 kyr), and (4) shoreward contraction of the
31 upwelling filament, and decreased upwelling strength over most of the uppermost
32 bathypelagic (19 kyr – 6 kyr). The latitudinal migration of the Southern Hemisphere
33 westerlies and the consequent contractions and expansions of the subpolar gyre played a
34 significant role in millennial and submillennial variability of SST off Namibia. The strength
35 of the southeasterly trade winds, rapid sea-level variations and the equatorward leakage of
36 Antarctic silicate might have acted as amplifiers. Although late Quaternary variations of
37 productivity and upwelling intensity in eastern boundary current systems are thought to be
38 primarily linked to the variability in wind stress, this multi-parameter reconstruction shows

39 that interplaying mechanisms defined the temporal variation pattern of the filament front
40 migrations and the diatom production off Namibia during the past 70 kyr.

41

42 Key words: Benguela, diatoms, millennial and submillennial time scale, productivity, sea-
43 surface temperature, SW Atlantic, upwelling filaments.

44

45 1. Introduction

46 Due to intense upwelling and strong nutrient recycling, primary productivity variations of
47 eastern boundary current systems play a significant role in regulating the present-day CO₂
48 content of the atmosphere (Longhurst et al., 1995). Among these high productive marine
49 coastal areas, the Benguela Upwelling System (BUS) along SW Africa is spatially one of the
50 present-day largest systems (Shannon, 1985). The BUS exhibits a range of filaments (narrow
51 protuberances extending from main upwelling zone, see below Section 2) and frontal
52 meanders that represent an effective mechanism for nutrient export from the productive inner
53 shelf to the less nutrient-rich pelagic realm (Shillington, 1998). The spatial area covered by
54 filaments along the South African and Namibian coast is more extensive than that of the
55 proper coastal upwelling (Lutjeharms and Stockton, 1987). The up-to-750 km seaward
56 transport of nutrients and microorganisms affects the dynamics and the intensity of the
57 primary productivity over most of the continental slope and the pelagic Atlantic off SW
58 Africa (Shillington, 1998). Hence, it is conceivable that a substantial or even a major portion
59 of the total primary production attributable to the upwelling dynamics takes place in the
60 filaments and not along the coastal upwelling region (Lutjeharms and Stockton, 1987).

61 As known from similar coastal upwelling settings (*e.g.*, off NW Africa and off Peru;
62 Romero et al., 2008; Romero and Armand, 2010), the current heterogeneous spatial
63 distribution of nutrients in the BUS causes a marked east-west primary productivity gradient

64 off SW Africa (Shannon, 1985; Lutjeharms and Stockton, 1987). Due to the strong spatial
65 heterogeneity of hydrography and atmospheric conditions off SW Africa, generalized
66 statements on paleoproductivity based on only one core location have proven to be
67 insufficient (Mollenhauer et al., 2002). The combined effect of a productivity gradient and
68 increasing water depth with increasing distance from the shoreline resulted in variable
69 sedimentation patterns during the late Quaternary along the SW African coast (Mollenhauer et
70 al., 2002; Pichevin et al., 2005a, b; Romero, 2010). Whether the offshore transport of
71 nutrients from the Namibian coastal area upon the pelagic realm had any effect on the long-
72 term paleoproductivity has still to be demonstrated.

73 Following the fact that modern enhanced productivity concentrates at the filament front
74 (Lutjeharms and Stockton, 1985), we hypothesize that past variations of the front location and
75 primary productivity intensity should be recognized in downcore sediments. By comparing
76 micropaleontological and geochemical data from two sediment cores, we were able to
77 reconstruct past migrations of the filament front location and assessed their effects on primary
78 productivity over the past 70 kyr. We generated micropaleontological (diatoms) and
79 geochemical (calcium carbonate, organic carbon, opal, $\delta^{18}\text{O}$ of benthic foraminifera, and
80 alkenone-based sea surface temperatures (SST)) data for core MD96-2098 (off Lüderitz,
81 Namibia, Fig. 1). These records were compared with those previously published from the
82 nearby core GeoB3606-1 (Romero, 2010). In addition, we obtained a new submillennial-
83 resolved alkenone SST record for core GeoB3606-1. Owing to the longitudinal geographical
84 distance between both drill sites (ca. 26 nautical miles = ca. 50 km), the two studied core sites
85 are located in the present-day back-and-forth migration front of one of the most productive
86 and dynamic BUS filaments (Shannon, 1985; Lutjeharms and Stockton, 1987). Site MD96-
87 2098 is located in the less productive zone, beyond the present-day outermost border of the
88 filaments at 26°-25°S off Lüderitz (Fig. 1), while site GeoB3606-1 is located in the middle-
89 slope, presently mostly beneath or close to the more productive surface waters overlying the

90 upper and middle continental slope. The comparison of the new and published data allows us
91 to build a coherent, synoptic picture of past changes in productivity in the Lüderitz area,
92 addressing issues such as variations in the filament extensions/contractions, the intensity of
93 the upwelling, and the nutrient availability in the central BUS during the past 70 kyr.

94

95 2. Modern oceanographic and climatic settings

96 The BUS extends along the SW African margin, adjacent to the coast of Angola, Namibia
97 and South Africa. Its northern and southern boundaries are defined as the Angola-Benguela
98 Front and the Agulhas retroflexion, respectively (Lutjeharms and Meeuwis, 1987). The
99 present-day wind field off SW Africa is dominated by the trade winds, which cause the
100 occurrence of upwelling in austral spring and summer off Lüderitz (Shannon and Nelson,
101 1996). Prevailing southeasterly trade winds drive the upwelling of cold and nutrient-rich
102 waters originating from depths between 150 and 330 m (roughly corresponding to the South
103 Atlantic Central Water, Shannon, 1985, and references therein).

104 The SE Atlantic upwelling regime consists of a spatially continuous coastal upwelling
105 strip, as well as an offshore area consisting of several mesoscale features. Off Lüderitz (25°-
106 26°S), these features (a collection of plumes, streamers, eddies and filaments; Lutjeharms and
107 Stockton, 1987) exhibit a tendency to extend farther offshore than further north and further
108 south. For this study, the term “filament” is used for narrow (<50 km) protuberances
109 extending more than 50 km from the main thermal upwelling front and being narrower than
110 50 km. Such filaments occasionally coalesce to form a much wider amalgamated feature,
111 which is hereafter referred to as an upwelling plume (Lutjeharms and Stockton, 1987).
112 Plumes are also formed in other ways than the product of filament fusion.

113 Based on their spatial and temporal variability and their relationships to wind forcing, 12
114 main coastal upwelling cells have been identified in the upwelling regime off southern

115 Africa's west coast (Lutjeharms and Meeuwis, 1987). Among them, the region around
116 Lüderitz (25°-26°S, Fig. 1) region was identified already in the early 1950s as an important
117 upwelling site (Shannon, 1985, and references therein). An analysis of present-day mean SST
118 found in each upwelling cell shows that there exists a well-behaved, latitudinally determined,
119 thermal relationship: mean SST decreases from north to south to the latitude of Lüderitz after
120 which it increases monotonically northwards (Lutjeharms and Meeuwis, 1987). Along the SW
121 African margin, the most frequent upwelling events, the furthest offshore extension of the
122 filament, and the highest frequency of occurrence of filaments occur off Lüderitz (Lutjeharms
123 and Meeuwis, 1987).

124 The thermal front off Lüderitz, coincident with the shelf break, demarcates the seaward
125 extent of upwelled waters. This front is highly convoluted, often disturbed by small filaments
126 and eddies, and extends seaward as far as 750 km (Lutjeharms and Meeuwis, 1987). On the
127 offshore side of the front, secondary upwelling may occur. Since the development of the
128 extensive and highly convoluted field of filaments, eddies, and thermal fronts is favorable for
129 high productivity (Shannon, 1985, and references therein), enhanced phytoplankton
130 productivity does not often occur in the center of upwelling cells, but rather offshore and at
131 the borders, or just outside, of upwelling centers (Lutjeharms and Stockton, 1987, and
132 references therein). With the onset of winter the Namibia upwelling cell and the filamentous
133 components are strongly developed (Lutjeharms and Meeuwis, 1987). Though clearly present
134 throughout the year, the Lüderitz cell is thermally most intense during fall, broadening its
135 alongshore extent into the Walvis area in winter and spring. This seasonal pattern is mirrored
136 by pigment concentration in surface waters (Fig. 1).

137 The maximum wind stress over the Lüderitz upwelling system lies in a band offshore,
138 which lays some 200-300 km offshore. Together with wind-stress patterns, the bottom
139 topography possibly determines the axes angles of the upwelling system. The axis orientation

140 observed in the upwelling filaments shows increasing trend to east-west zonality off Lüderitz
141 (Lutjeharms and Stockton, 1987, and references therein).

142 3. Material and Methods

143 3.1. Core location

144 Piston core MD96-2098 (25°35.99'S, 12°37.79'E, 2910 m water depth) was collected off
145 Namibia (Fig. 1) during Images II – NAUSICAA cruise on R/V Marion Dufresne II
146 (Bertrand, 1997). Gravity core GeoB3606-1 (core length = 1074 cm; 25°28.0'S, 13°05.0'E;
147 Romero, 2010) was collected on R/V METEOR cruise 34/1 from a water depth of 1785 m on
148 the continental slope of the Cape Basin (Fig. 1).

149 3.2. Stratigraphy and sampling

150 The stratigraphy for core MD96-2098 bases on oxygen isotope analyses on shells of the
151 benthic foraminifera *Cibicidoides wuellerstorfi* and was previously presented by Pichevin et
152 al. (2005a). For our research, we constructed a new chronology by tuning the available $\delta^{18}\text{O}$
153 record from MD96-2098 to the *Globigerina inflata* $\delta^{18}\text{O}$ from core GeoB1711-4 (12.37°S,
154 23.32°E, Kirst et al., 1999; Romero, 2010). The last 34,000 years from Core 1711-4 are also
155 dated by seven AMS¹⁴C measurements, giving good age constraints for the top part of the
156 core. We choose eight tie points between both records for the past 140 kyr. These tie points
157 were chosen because they are well-described climatic events and well expressed in both $\delta^{18}\text{O}$
158 records (for instance: the beginning of the Holocene plateau (10 kyr), beginning of the last
159 deglaciation (18 kyr), maxima in MIS 3, MIS 4, MIS 5c and 5e, Termination II). The core top
160 was estimated by comparing the $\delta^{18}\text{O}$ of both cores and is only a rough estimate in the
161 absence of ¹⁴C dates. This interpretation does not undermine our interpretations.

162 The total length of core MD96-2098 is 3224 cm. In this study, we presented results for the
163 upper 1000 cm (6-70 kyr) except for the alkenone analysis that was performed only in the
164 uppermost 460 cm. For the studied time interval, the sedimentation rate (SR) ranged between

165 ~8 and ~43.5 cm kyr⁻¹ (Fig. 2). SR remained above 10 cm kyr⁻¹ for most of the studied period
166 and reached its highest values (44 cm kyr⁻¹) between 520 and 250 cm (24–18 kyr) (Fig. 2).
167 Depending on the sedimentation rates, sampling resulted in temporal resolution varying
168 between ~100 years and ~1000 years for diatom counts and bulk geochemical and isotope
169 analyses and between ~1000 years and ~3000 years for alkenone analyses.

170 The age model for core GeoB3606-1 has been published elsewhere (Romero, 2010). The
171 published conventional radiocarbon (¹⁴C) ages for GeoB3606-1 were converted to calendar
172 ages, considering the ocean average of 400-yr reservoir age (Romero, 2010). Core
173 GeoB3606-1 was sampled every 5 cm, allowing analyses to be carried out at an average
174 sample interval ranging between 100 years and 250 years.

175 3.3. Diatoms

176 3.3.1. Sample preparation and census of valves

177 Diatom slides were prepared following the protocol by Rathburn et al. (1997).
178 Identification and counts were performed using an Olympus BH2 photomicroscope (EPOC,
179 Talence, France) at x1000 magnification. Three coverslips per sample were examined.
180 Following the counting procedure described in Crosta and Koç (2007), a minimum of 300
181 valves per slide were identified and counted. Several traverses across each coverslip were
182 studied, depending on the valve abundance. Diatoms were identified to species or species
183 group level. Species identification mainly follows Sundström (1986), Moreno-Ruiz and Licea
184 (1994), Moreno et al. (1996), and Hasle and Syversten (1997). The relative abundance (%) of
185 each species was determined as the fraction of the diatom species versus the total diatom
186 abundance in a particular sample.

187 Diatom accumulation rates were calculated with the following equation:

$$188 \text{ DAR} = (N_v * \text{WBD} * \text{SR}) / 2$$

189 where DAR is the diatom accumulation rate in millions $\text{cm}^{-2} \text{kyr}^{-1}$, N_v is the number of
190 diatom valves per gram of dry sediment, WBD is the wet bulk density in g cm^{-3} , and SR is the
191 sedimentation rates in cm kyr^{-1} .

192 3.3.2. Ecology of diatoms

193 To simplify the analysis of the paleoecological information of the diverse diatom
194 community (ca. 40 species identified in core MD96-2098), species sharing similar ecology
195 were lumped together. Based on habitats, nutrients and SST requirements, previous
196 investigations on diatom distribution in surface waters and in surface sediments from low-
197 latitude coastal and hemipelagic marine environments (Romero et al., 2002; Romero et al.,
198 2005; Romero and Armand, 2010) have demonstrated that it is useful to combine diatom
199 species in several groups to better understand paleoecological changes (e.g., Crosta et al.,
200 2012, Romero et al., 2011, 2012). The build-up of groups was based on simple comparison of
201 relative abundances or statistical approaches.

202 We defined four main diatom groups: pelagic-oligotrophic, coastal planktonic, upwelling,
203 and benthic. Marine pelagic-oligotrophic diatoms thrive in warm, nutrient-poor surface waters
204 with low siliceous productivity. At site MD96-2098, the pelagic-oligotrophic group is mainly
205 composed by large and well-silicified centric diatoms –such as *Azpeitia* spp., *Planktoniella*
206 *sol*, *Pseudosolenia calcar-avis*, *Rhizosolenia* spp., and *Thalassiosira* spp. with lesser
207 contribution by pennate forms such as *Nitzschia* spp. and *Thalassionema bacillaris*.

208 Coastal planktonic diatoms thrive in nutrient-rich coastal marine environments. This group,
209 which tracks high dissolved silica contents, non-upwelling conditions and low turbulence
210 waters, is composed at site MD96-2098 by several large and well silicified centric diatoms
211 such as *Actinocyclus* spp., *Actinoptychus* spp., *Coscinodiscus* spp., and the pennate
212 *Fragilariopsis doliolus*.

213 Upwelling diatoms thrive in surface waters with high dissolved silica concentrations and/or
214 high rate of nutrient replenishment to sustain blooming conditions. At site MD96-2098, this

215 group is dominated by resting spores *Chaetoceros* spp. and *Thalassionema nitzschioides* var.
216 *nitzschioides*. These species are abundant in areas of coastal or front filament upwelling,
217 though they can also reach high abundances in eutrophic environments with suitable
218 concentrations of Si and Fe (Romero and Armand, 2010).

219 Benthic diatoms occur attached to a substratum (rocks, sand, mudflats, macrophytes, etc.),
220 occur predominantly in shallow (< 50 m), marine to brackish waters of coastal marine zones
221 and river mouths, and track the transport from the coast and/or river mouth towards
222 hemipelagic and pelagic waters (Romero, 2010; Romero and Armand, 2010). At site MD96-
223 2098, pennate diatoms (particularly marine *Cocconeis* spp.) contribute the most.

224 3.4. Bulk geochemical analyses

225 We used absorbance mid-infrared spectroscopy in transmission mode at the Museum
226 National d'Histoire Naturelle (Paris, France) as a quantitative method to determine biogenic
227 opal concentration in MD96-2098. In given conditions (described below), the amount of
228 absorbed radiation is proportional to the quantity of absorbing matter in the sample (Bertaux
229 et al., 1998). Samples for opal measurements were mechanically ground with small agate
230 balls in an agate vial. Particle size of less than 2 mm is required to avoid excessive scattering
231 of IR radiation. The powder then was carefully mixed with KBr in an agate mortar. A dilution
232 of 0.25% was used for all samples studied. Pellets (300 mg, 13 mm in diameter) were
233 prepared by pressing the mixture in a vacuum die, applying up to 8 tons cm⁻² of compression.
234 The pellets were oven-dried for two days before data acquisition. IR spectra were recorded on
235 a Perkin-Elmer FT 16 PC spectrometer in the 4000–250 cm⁻² energy range with a 2 cm⁻²
236 resolution. For each spectrum, 50 scans were cumulated. Absorbance was computed relative
237 to a blank (pure KBr pellet). To determine biogenic opal concentration, the area of the opal
238 absorbance peak was multiplied by its specific absorbance coefficient k of 0.205.

239 Calcium carbonate (CaCO_3) measurements were performed applying a gasometric method.
240 Total organic carbon (TOC) measurements were performed on a LECO C-S 125 analyser at
241 EPOC (Talence, France) after treatment of the sediment with hydrochloric acid to remove
242 CaCO_3 . For both analyses, the precision was around 5%, expressed as the coefficient of
243 variation of replicate determinations.

244 3.5. Alkenone analyses and SST estimations

245 The SST estimates were based on alkenone measurements. Long-chain unsaturated ketones
246 for MD96-2098 were extracted and analysed by gas chromatography at EPOC, following the
247 methodology described by Villanueva and Grimalt (1997). To determine past SST variations
248 for GeoB3606-1, alkenones were extracted from 1-2 g portions of freeze-dried and
249 homogenized sediment at MARUM (Bremen, Germany) following the procedure described
250 by Kim et al. (2002). The extracts were analyzed by capillary gas chromatography using a gas
251 chromatograph (HP 5890A) equipped with a 60 m column (J&W DB1, 0.32 mm x 0.25 μm),
252 a split injector (1:10 split modulus), and a flame ionization detector. Quantification of the
253 alkenone content was achieved using squalane as an internal standard.

254 The alkenone unsaturation index $U_{37}^{K'}$ was calculated from $U_{37}^{K'} = (C_{37:2}) / (C_{37:2} + C_{37:3})$ as
255 defined by Prahl and Wakeham (1987), where $C_{37:2}$ and $C_{37:3}$ are the di- and tri-unsaturated
256 C_{37} methyl alkenones. The $U_{37}^{K'}$ values were converted into temperature values applying the
257 culture calibration of Prahl et al. (1988) ($U_{37}^{K'} = 0.034 * T + 0.039$), which has also been
258 validated by coretop compilations (Müller et al., 1998). The precision of the measurements (\pm
259 1σ) was better than 0.003 $U_{37}^{K'}$ units (or 0.1°C), based on multiple extractions and analyses of
260 a sediment sample used as a laboratory internal reference from the South Atlantic.

261

262 4. Results

263 4.1. Diatoms

264 At site MD96-2098, total diatom accumulation rate ($\text{diatom}_{\text{AR}}$) ranged between 1.2×10^8
265 and 4.7×10^9 valves $\text{g}^{-2} \text{kyr}^{-1}$ (average = 1.1×10^9 valves $\text{g}^{-2} \text{kyr}^{-1}$). Highest $\text{diatom}_{\text{AR}}$ ($>2.0 \times$
266 10^9 valves $\text{g}^{-2} \text{kyr}^{-1}$) occurred at 33,5 kyr, 31-29 kyr, 27-25 kyr and during the LGM (Fig. 3a).
267 Minor peaks were observed at 52 kyr, 46-44 kyr, and 37,5-37 kyr. Lowest $\text{diatom}_{\text{AR}}$ ($<0.4 \times$
268 10^9 valves $\text{g}^{-2} \text{kyr}^{-1}$) occurred during the late MIS4, the MIS4/MIS3 transition, and from the
269 deglaciation until ca. 6 kyr.

270 The diatom assemblage preserved in core MD96-2098 was highly diverse (number of
271 species identified = ~40). The upwelling group (see 3.3.2.) dominated (>80 % of relative
272 contribution) the total assemblage from 70 kyr until ca. 17 kyr, when the most important
273 temporal switch in the species composition occurred (Fig. 4). Two rapid decreases in relative
274 abundances of the upwelling group occurred at 60-57 kyr and 49-45 kyr.

275 Over the past 70 kyr, the contribution of pelagic-oligotrophic, benthic and coastal
276 planktonic diatoms followed an inverse pattern than that of upwelling diatoms: contribution of
277 the non-upwelling groups was high at 57-55 kyr and 52-48 kyr, and increased rapidly after 17
278 kyr into the mid Holocene. However, respective contributions showed different patterns
279 during the considered intervals. The pelagic-oligotrophic group was dominant between 17 kyr
280 and 10 kyr (deglaciation), while coastal planktonic diatoms were most abundant between 57-
281 55 kyr and 52-48 kyr, and after 8 kyr until the late Holocene. Benthic diatoms were most
282 abundant between 13 kyr and 8 kyr.

283 4.2. Bulk geochemical components

284 CaCO_3 was the dominant bulk biogenic component in MD96-2098 sediments, followed by
285 opal and TOC. For the studied period, the content of CaCO_3 fluctuated between 21.1 % and
286 82.4 % (average = 42.4 %) (Fig. 3b). CaCO_3 had highest values between 16 kyr and 6.3 kyr.
287 Secondary maxima occurred at 70-69 kyr, 51-50 kyr, 42 kyr and 38 kyr. Content of CaCO_3

288 was lowest in 62-58 kyr, 45-44 kyr, 35-33 kyr, and 30-26 kyr. Opal values varied between
289 3.4 wt. % and 21.7 wt. % (average = 10.7 wt. %) (Fig. 3c) The greatest contribution of opal
290 occurred between late MIS4 and early MIS3 (until ca. 42 kyr), and from mid MIS3 (37 kyr)
291 through the late deglaciation (ca. 11 kyr). The relative content of TOC ranged from 0.9 wt. %
292 to 6.2 wt. % (average = 4.2 wt. %) (Fig. 3d). TOC values remained above 4 wt. % between 61
293 kyr and ca. 15 kyr, with highest values occurring between 44 kyr and 15 kyr, and decreased
294 abruptly afterward into the mid Holocene.

295 4.3. Benthic $\delta^{18}\text{O}$

296 The $\delta^{18}\text{O}$ record of the benthic foraminifera *Cibicidoides wuellerstorfi* at site MD96-2098
297 exhibited substantial amplitude changes (~ 4.42 to 2.17 ‰, average 3.65 ± 0.57) (Fig. 3e).
298 Isotopic values ranged from 4.1 ‰ to 3.1 ‰ between 65 kyr and 26 kyr. A moderate
299 enrichment (3.79 - 4.39 ‰) occurred during the LGM. A decrease of almost 2 ‰ in $\delta^{18}\text{O}_{\text{benthic}}$
300 values is observed between late MIS2 and the mid Holocene.

301 4.4. Alkenone-derived SST

302 At the core site MD96-2098, for the interval 30.5-7 kyr, the low-resolution U_{37}^{K} record
303 revealed an amplitude change of ca. 5°C (range = $13.2 - 18.3^\circ\text{C}$, average $15.2 \pm 1.6^\circ\text{C}$) (Fig.
304 3f). Lowest SSTs occurred between 28 kyr and 19 kyr. A warming of ca. 3°C occurred around
305 15.5 kyr. Early Holocene SSTs remained above 17°C .

306 The high-resolution U_{37}^{K} record of GeoB3606-1 showed that SSTs over the Lüderitz mid-
307 slope were highly variable (range 12.0 - 18.1°C , average $14.9 \pm 1.5^\circ\text{C}$), and recorded numerous
308 substantial shifts throughout the past 70 kyr (Fig. 3f). The most prominent submillennial-scale
309 shift of ~ 1 - 2°C occurred between 70 kyr (late MIS4) and 45.5 kyr (mid MIS3). Lowest SST
310 for the entire study interval occurred between 45 kyr and 40 kyr, followed by a rapid warming
311 at 39-38 kyr. After the cooling at 37.5-34.5 kyr, submillennial-scale variations of SST
312 persisted. SST increased by 3°C from 34 kyr until 28.5 kyr. During the LGM, the SST

313 presented small amplitude variations between 16.2°C and 15.5°C. A moderate cooling (16.4-
314 16.6°C) occurred between 16 kyr and 14 kyr. For most of the Holocene, SST varied between
315 17.3°C and 18.1°C.

316

317 5. Discussion

318 We compared the records gained at the continental rise site MD96-2098 (water depth 2,910
319 m) with those previously generated at the nearby site GeoB3606-1 (water depth 1,785 m;
320 Romero, 2010). This comparison allowed us to address the relationship between the location
321 of the main diatom production centre in frontal waters of the Lüderitz filament and the
322 variability of upwelling intensity and Antarctic-derived Si at 25°-26°S off Namibia over the
323 past 70 kyr.

324 5.1. Longitudinal expansions and contractions of the Lüderitz filament

325 Based on the knowledge that present-day primary productivity is enhanced at the filament
326 front off Lüderitz and that frontal productivity forms a significant proportion of the total
327 productivity of an upwelling cell (see above Section 2.), we argue that late Quaternary
328 variations in productivity recorded in our sedimentary records allowed us to reconstruct past
329 shifts in the front position. We propose that the seaward-shoreward (*i.e.* westward-eastward)
330 migrations of the Lüderitz filament front at 25°-26°S occurred in four main phases as
331 described below (Fig. 5).

332 5.1.1. Phase 1 (late MIS4 to mid MIS3, 70-44 kyr) – Main upwelling front over the mid-slope 333 off Lüderitz

334 Between 70 kyr and 44 kyr, lower values of diatoms, opal and TOC at site MD96-2098
335 than at site GeoB3606-1 (Fig. 3) suggested less intense upwelling and lower productivity in
336 deeper pelagic waters than over the mid-slope off Lüderitz. Although the synchronous
337 occurrence of upwelling over a large geographical area off Lüderitz is evidenced by the

338 dominance of upwelling diatoms at both sites (Fig. 4), upwelling was more intense over site
339 GeoB3606-1 than in waters overlying site MD96-2098. We primarily attribute the differences
340 in siliceous primary paleoproductivity between the studied sites to the location of the
341 outermost border of the Lüderitz filament, which was located closer to 13°E (GeoB3606-1)
342 than to 12°E (MD96-2098) until around 44 kyr. Secondly, the input of Si-rich waters above
343 site GeoB3606-1 determined the highs and lows of diatom production.

344 5.1.2. Phase 2 (mid to late MIS 3, 44-31 kyr) – Seaward displacement of the upwelling front

345 The increase of the total diatom concentration at site MD96-2098 around 38 kyr followed
346 the decrease in diatom production (Fig. 3a, c, d) and the moderate increase of pelagic-
347 oligotrophic taxa at site GeoB3606-1 around 44 kyr (Fig. 4). The diverse community of
348 upwelling-related *Chaetoceros* spores also responded to the decreased availability of nutrients
349 in waters overlying site GeoB3606-1 and switched from the dominance of high- to moderate-
350 productive water spores (Romero, 2010).

351 5.1.3. Phase 3 (late MIS 3 to LGM, 31-19 kyr) – Main upwelling front and diatom production
352 center overlying deeper pelagial waters

353 The increase of diatom productivity at site MD96-2098 in the late MIS 3 (Figs. 3a, 6g)
354 suggests the further seaward displacement of the outermost border of the upwelling front. No
355 particular shift in the species composition of the diatom assemblage accompanied the diatom
356 increase: *Chaetoceros* spores, typical of moderate upwelling intensity, dominated at site
357 GeoB3606-1 throughout until ca. 20-19 kyr (Romero, 2010). This suggests that the
358 hydrodynamic conditions for the occurrence of upwelling were present at both locations,
359 though Si availability was higher over site MD96-2098 than over site GeoB3606-1.

360 5.1.4. Phase 4 (deglaciation to mid-Holocene, 19-6 kyr) – Landward retraction of the Lüderitz
361 filament

362 The distinctive shift in the species composition – from an upwelling-dominated to a non-
363 upwelling community (Fig. 4) – and the increase of CaCO₃ values (Fig. 3b) occurred almost
364 simultaneously at both sites during the early deglaciation. This evidence supports the scenario
365 of the weakening of upwelling intensity over a broad part of the uppermost bathypelagial off
366 Lüderitz, the landward retraction of the outermost border of the filament and the occurrence
367 of Si-depleted waters.

368 5.2. Mechanisms and amplifiers responsible for the expansions and contractions of the 369 Lüderitz filament

370 Since waters at the outermost front of the Lüderitz filament are colder and more productive
371 than surrounding water masses (see 2.), rapid SST and diatom variations for the past 70 kyr
372 off Lüderitz can be interpreted as recording the migrations of the filament front location and
373 upwelling intensity. Mechanisms and amplifiers determining the seaward and shoreward
374 migration of the outermost filament front off Lüderitz are discussed below.

375 5.2.1. Atmospheric and hydrographic forcing of the filament front migration and the diatom 376 production off Lüderitz

377 The contractions and expansions of the Lüderitz filament mostly responded to Southern
378 Hemisphere-driven atmospheric and hydrographic changes. The strength and the latitudinal
379 position of the Southern Hemisphere westerlies and the concurrent extent of the subpolar
380 gyres might have acted as a potential trigger for the forcing of the offshore streaming of the
381 Lüderitz filament. The equatorward (poleward) expansion (contraction) of the Southern
382 Hemisphere subtropical gyres (Peterson and Stramma 1991; Beal et al., 2011) supply the
383 mechanistic setting for the advection of warm Agulhas Water sourced from the Indian Ocean
384 into the SE Atlantic Ocean. This transport might be an important step in initiating the frontal
385 breakdown along the southern BUS (Lutjeharms and Stockton, 1987). Previous studies
386 showed that the entrance of warm waters through the Indian-Atlantic Ocean Gateway – weak
387 between late MIS 4 and late MIS 2 (Fig. 6a) – strongly influenced the hydrology of the

388 southern BUS (Peeters et al., 2004; Beal et al., 2011). In support of this scenario, a numerical
389 experiment based on a global general circulation model (Sijp and England, 2008) suggests
390 that reduced leakage of Agulhas waters deprives the SE Atlantic of warm and saline Indian
391 Ocean waters, leading to the cooling and freshening of waters in the southern BUS. Based on
392 previous findings that the past position of the Southern Hemisphere westerlies exhibited
393 natural decadal variability (Sijp and England, 2008; De Deckker et al., 2012) and that the
394 hydrography around the southern tip of Africa has experienced strong millennial-scale
395 variability (Peeters et al., 2004; Marino et al., 2013; Simon et al., 2013), we argue that the
396 submillennial-scale coolings and warmings of alkenone-based SST at site GeoB3606-1
397 between 70 kyr and 27 kyr (Fig. 6e) responded to rapid contractions and expansions of the
398 outermost front of the Lüderitz filament.

399 In addition to the teleconnections between the SE Atlantic and the subpolar gyres, the
400 regional trade wind forcing along the Namibian coastal area at 25°-26°S might have amplified
401 the sub-Milankovitch scale pattern of migration of the upwelling front location. Perennially
402 consistent trade winds off Lüderitz (Shannon and Nelson, 1996) allow the almost year-around
403 cooling and fertilization of surface waters of the Lüderitz filament (see above Section 2.).
404 Sedimentological studies conducted on the upper slope core MD96-2087 (25.6°S, 13.38°E,
405 1029 m water depth) showed that the mean grain size of dust particles supplied to the ocean
406 floor of the coastal SE Atlantic during the late Quaternary might be a reliable indicator of the
407 aridity of the Namibian desert – the main dust source area for the study area – and of the wind
408 strength in the neighboring Namibian upwelling (Fig. 6c; Pichevin et al., 2005b). The strong
409 match between windier conditions and the overall trend of highest diatom values at site
410 GeoB3606-1 from 65 kyr to 38 kyr is evidence of the trade wind effect on the diatom
411 production. Some mismatches between the SST record and the MD96-2087 wind record are
412 possibly due to different sampling resolution (lower at site MD96-2087) and stratigraphic
413 differences between both cores. Similarly, the increase of SST at both sites MD96-2087 and

414 GeoB3606-1 (Fig. 6d, e) corresponds well the weakened trades intensity after 39 kyr (Fig. 6c,
415 arrow).

416 The cooling between 23 and 19 kyr (Fig. 6d, e) was possibly due to more intense trade
417 winds during the LGM (as evidenced by larger mean grain sizes between ca. 24 kyr and 19
418 kyr, Fig. 6c). In addition to the glacial equatorward shift of the Southern Hemisphere
419 westerlies (Sijp and England, 2008), the stronger trades might have pushed the filament front
420 beyond surface waters overlying site GeoB3606-1 further out into more open-ocean waters.
421 Following strengthened winds, the increased mixing and the injection of cold thermocline
422 waters into the uppermost 20-to-40 m of the water column occurred over site MD96-2098
423 during the LGM, leading to high diatom production (Figs. 3a, 6g).

424 The simultaneous warming recorded along 25°-26°S during the last deglaciation (19-13
425 kyr) (Figs. 4e, 6d, e) provided a robust evidence for the shoreward retraction of the outermost
426 border of the filament and the enhanced stratification of the uppermost water column over a
427 large area off Lüderitz. This scenario is supported by the distinctive shift in the species
428 composition of the diatom assemblage from an upwelling-dominated to a non-upwelling
429 community over both study (Fig. 4), and the increase of CaCO₃ – indicative of increased
430 calcareous productivity – values by the late MIS2 (Fig. 3b) that evidenced major changes in
431 nutrient availability off Lüderitz. During the last deglaciation, the Southern Hemisphere
432 westerlies weakened (Sijp and England, 2008) and the expansion of the gateway between
433 southern Africa and the Southern Hemisphere Subtropical Front allowed increased leakage of
434 Agulhas waters into the southern BUS (Fig. 6a; Peeters et al., 2004), which contributed to the
435 warming of surface waters off Lüderitz.

436 5.2.2. Sea-level variations as a potential amplifier of the filament front migration

437 Sea level variations have been put forth as a possible explanation of variations of filaments
438 fertility in low-latitude coastal upwelling areas (Bertrand et al., 2000; Giraud and Paul, 2010).
439 Four main intervals of sea level fluctuations with magnitudes between -10 m and -120 m

440 correspond with the time window covered by cores GeoB3606-1 and MD96-2098 (Fig. 6b).
441 The interval of highest diatom values at site GeoB3606-1 between 68 kyr and 44 kyr match a
442 sea-level stand of 60-to-90 m lower than today. This lowering of the Namibian coastline
443 contributed to displace the filament front closer to site GeoB3606-1 (Fig. 5), where upwelling
444 rapidly varied between silica-rich and silica-depleted stages (see below Section 5.2.3.).

445 The second interval of sea level low-stand started around 44 kyr with a two-step decrease
446 (Fig. 6b, arrows A and B). This decrease was concurrent with the increase of SST at core
447 MD96-2087 (Fig. 6d) suggesting that the further lowering of sea level pushed the outermost
448 filament seaward. Despite the fact that SST data for core GeoB3606-1 have higher resolution
449 than those for the shallower MD96-2087, the overall pattern of temperature oscillations
450 matches well between both localities (Fig. 6d, e), this being good indicator of the longitudinal
451 migration of the filament front. Siddall et al. (2008) stated, however, that rapid sea level
452 changes during MIS 3 might not have followed systematic, repeating patterns. We do not
453 argue here that the millennial-to-submillennial SST variability at GeoB3606-1 fully followed
454 the rapid sea level variations, but rather that the timing of sea level fluctuations amplified the
455 intensity of upwelling determined by atmospheric and hydrological changes in the southern
456 BUS.

457 During the LGM low-stand (third sea level interval), the Namibian coastline position
458 lowered again by many tens of kilometers (Fig. 5), which might have acted as an amplifier by
459 shifting the outermost front of the Lüderitz filament further out upon the pelagic realm. The
460 lowest sea level stand, that exposed large areas close to the coastal environment during the
461 LGM, did not compensate for the decrease induced by the reduced subsurface nutrient
462 concentration over site GeoB3606-1.

463 Because of the sea level change along the Namibian coast after the LGM (Fig. 6b), it is
464 tempting to argue that the rise of sea level during the last deglaciation shifted the filament
465 front location closer to the Namibian coastline. Both study sites GeoB3606-1 and MD96-2098

466 were not in the same position relative to the maximum production center of the filament front
467 upwelling, which became closer to closer to the Namibian coastline.

468 5.2.3. Availability of Antarctic-leaked Si off Lüderitz

469 Several short intervals of total diatom maxima matched marked sea surface coolings over
470 the upper- (MD96-2087) and mid-slope (GeoB3606-1) off Lüderitz between 70 kyr and 27
471 kyr (Fig. 6d, e). On the other hand, episodes of diatom minima –dominated also by upwelling
472 species (Fig. 4)– matched moderate-to-high SST (Fig. 6d, f). SST coolings and strong mixing
473 of the uppermost water column alone cannot fully explain variations in total diatom
474 concentration and shifts in the species composition. We postulate that changes in the Si
475 content of BUS surface waters determined the occurrence of two types of upwelling off
476 Lüderitz: silicate-rich vs. silicate-poor.

477 The occurrence of the Antarctic diatom *Fragilariopsis kerguelensis* in sediments of the
478 southern BUS has been proposed to trace the advection of Si-rich, Antarctic-originated waters
479 into the low-latitude SE Atlantic (Romero, 2010). Between 70 kyr and ca. 30 kyr, the inverse
480 correlation between the relative abundance of *F. kerguelensis* (Romero, 2010) and the SST
481 variations (*i.e.* highest *F. kerguelensis* values matched lowest SST) at the millennial scale
482 suggested high availability of dissolved Si in upwelling waters. We postulate that intermittent
483 pulses of Si into the BUS led to the upwelling of Si-rich waters. This nutrient scenario was
484 triggered by the equatorward transport of Si-enriched waters of Antarctic origin, either by
485 direct mixing or by the advection of Subantarctic Mode Waters (whose present-day Si content
486 is low relative to surrounding water masses; Matsumoto et al., 2002) that invaded the middle
487 to lower thermocline of subtropical coastal upwelling areas (Sarmiento et al., 2004). The
488 equatorward leakage of dissolved Si followed intervals of lowered diatom productivity in the
489 Southern Ocean south of the Subantarctic Front due of varying physical and biological
490 conditions (sea ice cover, winds, Fe input) (Matsumoto et al., 2014). Two possible drawbacks
491 of this sub-Milankovitch scale leakage scenario are the lack of a diatom reconstruction south

492 of the Subantarctic Front showing millennial-scale variability, and the prediction of glacial
493 increases and interglacial decreases of Si leakage (Brzezinski et al., 2002; Bradtmiller et al.,
494 2009). In addition to bioavailable Fe fertilization (Brzezinski et al., 2002; Matsumoto et al.,
495 2002), a recent model simulation experiment suggested that sea ice cover and the intensity of
496 subpolar southern westerlies can also trigger the equatorward leakage of Si and that the
497 biogeochemical response to each of the three triggers –not mutually exclusive– is different
498 (Matsumoto et al., 2014). Additional evidence for a non-glacial, sub-Milankovitch Si leakage
499 is provided by increased opal burial recorded in the eastern equatorial Pacific between 40-60
500 kyr, attributed to extended sea ice around Antarctica (Kienast et al., 2006). The diatom
501 maxima at MD96-2098 during the MIS 3/2 transition and the LGM followed the leaked Si
502 due to limited diatom production south of the Polar Front (Chase et al., 2003) as a
503 consequence of the widely extended sea ice cover between ca. 25 kyr and 18 kyr (Crosta et
504 al., 2005). The further lowering of the sea level around 27 kyr (Fig. 6b, arrow B, see
505 discussion above) might have amplified this signal by pushing the outermost border of the
506 Lüderitz filament closer to MD96-2098.

507 The decreased Si delivery into the SE Atlantic after 19 kyr led to the almost simultaneous
508 floral shift at both MD96-2098 and GeoB3606-1. Calcite-secreting coccolithophorids became
509 dominant at the expense of silica-bearing diatoms. Higher CaCO₃ (lower opal) values at both
510 sites from late MIS2 to the mid/late Holocene (Fig. 5b, c) indicated a shift in predominant
511 nutrients toward Si-depleted waters over a wide area off Lüderitz. Following the lessened sea
512 ice cover (Crosta et al., 2005), and the lowered input of Fe south of the Polar Front due to
513 weakened wind intensity during the last deglaciation (Kohfeld et al., 2005; Sijp and England,
514 2008), Si was mainly consumed in waters south of the Subantarctic Front and became mostly
515 trapped in underlying sediments (Brzezinski et al., 2002; Matsumoto et al., 2002). This
516 scenario corresponds to the present-day dynamics of production and sedimentation of

517 biogenic particulates in the southern BUS (Romero et al., 2002; Romero and Armand, 2010),
518 where coccolithophorids dominate primary production over diatoms.

519

520 6. Conclusions

521 Based on the knowledge that present-day productivity is at its highest at the filament front,
522 we reconstruct past variations of front location off Namibia. Multi-parameter lines of
523 evidences from this study suggest that several mechanisms and amplifiers determined the
524 extension/contraction of the upwelling filament and the geographical location of the diatom
525 production center off Lüderitz over the past 70 kyr. Atmospheric (wind intensity) and
526 hydrographic/physical variability (surface and thermocline waters, SST and surface
527 stratification, sea level stand), and nutrient supply (Si input) determined the settings for
528 upwelling intensity and diatom production off Lüderitz. These mechanisms and amplifiers
529 might have been linked and not been mutually exclusive.

530 The discussed mechanisms and amplifiers responsible for the strong diatom and SST
531 fluctuations imply that the one-dimensional view of upwelling dynamics (downward flux of
532 biogenic material from the surface balanced by upwelling of dissolved inorganic nutrients
533 driven by vertical mixing of the thermocline) does not necessarily apply to the Lüderitz
534 filament front.

535 The interpretation of the sedimentary signal as a record of regional conditions cannot be
536 extrapolated to the entire BUS. Although our various proxies agree on details of the
537 reconstructed sub-Milankovitch time scale variations, some ambiguities still remain to be
538 explained. In this regard, further advances concerning mechanisms and amplifiers discussed
539 here should be included in numerical modelizations of abrupt fluctuations of productivity and
540 SST changes in low-latitude coastal upwelling systems. In particular, the possible impact of

541 millennial-to-submillennial sea level changes, nutrient supply and sources, wind strength and
542 their effect on productivity and CO₂ content for the past 70 kyr should be tested in the future.

543

544 Acknowledgements

545 Mr. J. Villanueva performed the U₃₇^{K'} measurements on MD96-2098 (EPOC, Talence,
546 France). OER was partially supported by the German Research Foundation (DFG). The
547 research leading to these results has received funding from the European Research Council
548 under the European Union's Seventh Framework Program (FP7/2007-2013) / ERC grant
549 agreement n° [226600], which financed JHK. Comments and suggestions by two anonymous
550 reviewers greatly improved a first version of this work. Data are available in the database
551 www.pangaea.de.

552

553 References

- 554 Beal, L.M., De Ruijter, W.P.M., Biastoch, A., Zahn, R., 2011. On the role of the Agulhas
555 system in ocean circulation and climate. *Nature* 472, 429–436.
- 556 Bertaux, J., Frohlich, F., Ildefonse, P. 1998. Multicomponent analysis of FTIR spectra:
557 Quantification of amorphous and crystallized mineral phases in synthetic and natural
558 sediments. *Journal of Sedimentary Research* 68, 440-447.
- 559 Bertrand, P. 1997. NAUSICAA – Images II MD 105 Cruise Report. Institut Français pour la
560 Recherche et la Technologie Polaire (IFRTP), Plouzané, France, pp. 1-381.
- 561 Bertrand, P., Pedersen, T.F., Martinez, P., Calvert, S., Shimmield, G., 2000. Sea level impact
562 on nutrient cycling in coastal upwelling areas during deglaciation: Evidence from nitrogen
563 isotopes. *Global Biogeochemical Cycles* 14, 341-355.

- 564 Bradtmiller, L.I., Anderson, R.F., Fleisher, M.Q., Burckle, L.H. 2009. Comparing glacial and
565 Holocene opal fluxes in the Pacific sector of the Southern Ocean. *Paleoceanography* 24,
566 PA2214, doi:10.1029/2008PA001693.
- 567 Brzezinski, M.A., Pride, C.J., Sigman, D.M., Sarmiento, J.L., Matsumoto, K., Gruber, N.,
568 Rau, G.H., Coale, K.H., 2002. A switch from Si(OH)₄ to NO₃ depletion in the glacial
569 Southern Ocean. *Geophysical Research Letters* 29, doi:1510.1029/2001GL014349.
- 570 Chase, Z., Anderson, R.F., Fleisher, M.Q., Kubik, P.W., 2003. Accumulation of biogenic and
571 lithogenic material in the Pacific sector of the Southern Ocean during the past 40,000
572 years. *Deep-Sea Research II* 50, 799-832.
- 573 Crosta, X., Shemesh, A., Etourneau, J., Yam, R., Billy, I., Pichon, J.J., 2005. Nutrient cycling
574 in the Indian sector of the Southern Ocean over the last 50,000 years. *Global*
575 *Biogeochemical Cycles* 19, doi:10.1029/2004GB002344.
- 576 Crosta, X., Koç, N., 2007. Diatoms: From micropaleontology to isotope geochemistry. In:
577 Hilaire-Marcel, C., de Vernal, A. (Eds), *Proxies in Late Cenozoic Paleooceanography*,
578 *Developments in Marine Geology Series, Volume 1*, Elsevier, Amsterdam, The
579 Netherlands, pp. 327–369.
- 580 Crosta, X., Romero, O.E., Schneider, R., Ther, O., 2012. Climatically-controlled siliceous
581 productivity in the eastern Gulf of Guinea during the last 40.000 years. *Climate of the Past*
582 8, 415–431.
- 583 De Deckker, P., Moros, M., Perner, K., Jansen, E. 2012. Influence of the tropics and southern
584 westerlies on glacial interhemispheric asymmetry. *Nature Geoscience* 5, 266-269.
- 585 Giraud, X., Paul, A., 2010. Interpretation of the paleo–primary production record in the NW
586 African coastal upwelling system as potentially biased by sea level change.
587 *Paleoceanography* 25, PA4224, doi:10.1029/2009PA001795.
- 588 Hasle, G.R., Syversten, E.E., 1997. Marine diatoms. In: Tomas, C.R., (Ed.), *Identifying*
589 *Marine Diatoms and Dinoflagellates*, Academic Press, San Diego, USA, pp. 5–385.

- 590 Kienast, S.S., Kienast, M., Jaccard, S., Calvert, S.E., François, R., 2006. Testing the silica
591 leakage hypothesis with sedimentary opal records from the eastern equatorial Pacific over
592 the last 150 kyrs. *Geophysical Research Letters* 33, L15607, doi:10.1029/2006GL026651.
- 593 Kim, J.-H., Schneider, R.R., Müller, P.J., Wefer, G., 2002. Interhemispheric comparison of
594 deglacial sea-surface temperature patterns in Atlantic eastern boundary currents. *Earth and*
595 *Planetary Science Letters* 194, 383-393.
- 596 Kohfeld, K.E., Le Quéré, C., Harrison, S.P., Anderson, R.F., 2005. Role of Marine Biology in
597 Glacial-Interglacial CO₂ Cycles. *Science* 308, 74-78.
- 598 Lisiecki, L.E., Raymo, M.E., 2007. Plio–Pleistocene climate evolution: trends and transitions
599 in glacial cycle dynamics. *Quaternary Science Reviews* 26, 56–69.
- 600 Longhurst, A.L., Sathyendranath, S., Platt, T., Caverhill, C., 1995. An estimate of global
601 primary production from satellite radiometer data. *Journal of Plankton Research* 17, 1245–
602 1271.
- 603 Lutjeharms, J.R.E., Meeuwis, J.M., 1987. The extent and variability of South-east Atlantic
604 upwelling. *South African Journal of Marine Sciences* 5, 51–62.
- 605 Lutjeharms, J.R.E., Stockton, P.K., 1987. Kinematics of the upwelling front off Southern
606 Africa. *South African Journal of Marine Sciences* 5, 35–49.
- 607 Marino, G., Zahn, R., Ziegler, M., Purcell, C., Knorr, G., Hall, I.R., Ziveri, P., Elderfield, H.,
608 2013. Agulhas salt-leakage oscillations during abrupt climate changes of the Late
609 Pleistocene. *Paleoceanography* 28(3): 599-606. doi: 510.1002/palo.20038.
- 610 Matsumoto, K., Sarmiento, J.L., Brzezinski, M.A., 2002. Silicic acid leakage from the
611 Southern Ocean: A possible explanation for glacial atmospheric *p*CO₂. *Global*
612 *Biogeochem. Cycles* 16, doi:10.1029/2001GB001442.
- 613 Matsumoto, K., Chase, Z., Kohfeld, K., 2014. Different mechanisms of silicic acid leakage
614 and their biogeochemical consequences. *Paleoceanography* 20, 238–254,
615 doi:210.1002/2013PA002588.

- 616 Mollenhauer, G., Schneider, R.R., Müller, P.J., Spieß, V., Wefer, G., 2002.
617 Glacial/Interglacial variability in the Benguela upwelling system: Spatial distribution and
618 budgets of organic carbon accumulation. *Global Biogeochemical Cycles* 16,
619 doi:10.1029/2001GB001466.
- 620 Moreno-Ruiz, J.L., Licea, S., 1994. Observations on the valve morphology of *Thalassionema*
621 *nitzschioides* (Grunow) Hustedt. In: Marino, D., Montresori, M. (Eds.), *Proceedings of the*
622 *13th Symposium on Living and Fossil Diatoms*. Biopress Limited Publisher, Bristol, U.K.,
623 pp. 393–413.
- 624 Moreno-Ruiz, J.L., Licea, S., Santoyo, H., 1996. *Diatomeas del Golfo de California*,
625 Universidad Autónoma de Baja California Sur, México, Mexico, pp. 1-203.
- 626 Müller, P., Kirst, G., Ruhland, G., von Storch, I., Rosell-Melé, A., 1998. Calibration of the
627 alkenone paleotemperature index U_{37}^K based on core-tops from the eastern South Atlantic
628 and the global ocean (60°N-60°S). *Geochimica et Cosmochimica Acta* 62, 1757–1772.
- 629 Peeters, F.J.C., Acheson, R., Brummer, G.-J.A., de Ruijter, W.P.J., Schneider, R.R., Ganssen,
630 G.M., Ufkes, E., Kroon, D., 2004. Vigorous exchange between the Indian and Atlantic
631 oceans at the end of the past five glacial periods. *Nature* 430, 661-665.
- 632 Peterson, R.G., Stramma, L., 1991. Upper-level circulation in the South Atlantic Ocean.
633 *Progress in Oceanography* 26, 1–73.
- 634 Pichevin, L., Martinez, P., Bertrand, P., Schneider, R.R., Giraudeau, J., 2005a. Nitrogen
635 cycling on the Namibian shelf and slope over the last two climatic cycles: Local and global
636 forcings. *Paleoceanography* 20, doi:10.1029/2004PA001001.
- 637 Pichevin, L., Cremer, M., Giraudeau, J., Bertrand, P., 2005b. A 190 kyr record of lithogenic
638 grain-size on the Namibian slope: Forging a tight link between past wind-strength and
639 coastal upwelling dynamics. *Marine Geology* 218, 81-96.

- 640 Prah1, F.G., Wakeham, S.G., 1987. Calibration of unsaturation patterns in long-chain ketone
641 compositions for paleotemperature assessment. *Nature* 330, 367–369.
- 642 Prah1, F.G., Muehlhausen, L.A., Zahnle, D.L., 1988. Further evaluation of long-chain
643 alkenones as indicators of paleoceanographic conditions. *Geochimica et Cosmochimica*
644 *Acta* 52, 2303–2310.
- 645 Rathburn, A.E., Pichon, J.-J., Ayres, M.A., DeDecker, P., 1997. Microfossil and stable-
646 isotope evidence for changes in Late Holocene paleoproductivity and paleoceanographic
647 conditions in the Prydz Bay region of Antarctica. *Palaeogeography, Palaeoclimatology,*
648 *Palaeoecology* 131, 485–510.
- 649 Rohling, E., Grant, K., Bolshaw, M., Roberts, A.P., Siddall, M., Hemleben, C., Kucera, M.,
650 2009. Antarctic temperature and global sea level closely coupled over the past five glacial
651 cycles. *Nature Geoscience* 2, 500–504.
- 652 Romero, O.E., Boeckel, B., Donner, B., Lavik, G., Fischer, G., Wefer, G., 2002. Seasonal
653 productivity dynamics in the pelagic central Benguela System inferred from the flux of
654 carbonate and silicate organisms. *Journal of Marine Systems* 37, 259–278.
- 655 Romero, O.E., Armand, L.K., Crosta, X., Pichon, J.-J., 2005. The biogeography of major
656 diatom taxa in Southern Ocean surface sediments: 3. Tropical/Subtropical species.
657 *Palaeogeography, Palaeoclimatology, Palaeoecology* 223, 49–65.
- 658 Romero, O.E., Kim, J.-H., Donner, B., 2008. Submillennial-to-millennial variability of diatom
659 production off Mauritania, NW Africa, during the last glacial cycle. *Paleoceanography* 23,
660 doi:10.1029/2008PA001601.
- 661 Romero, O.E., 2010. Changes in style and intensity of production in the Southeastern Atlantic
662 over the last 70,000 yr. *Marine Micropaleontology* 74, 15–28.
- 663 Romero, O.E., Armand, L.K., 2010. Marine diatoms as indicators of modern changes in
664 oceanographic conditions. In: Smol, J.P., Stoermer, E.F., (Eds.), *The diatoms: Applications*
665 *for the Environmental and Earth Sciences* (2nd Ed.). Cambridge University Press, U.K., pp.

- 666 373–400.
- 667 Romero, O.E., Leduc, G., Vidal, L., Fischer, G., 2011. Millennial variability and long-term
668 changes of the diatom production in the eastern equatorial Pacific during the last glacial
669 cycle. *Paleoceanography* 26, doi:10.1029/2010PA002099.
- 670 Romero, O.E., Mohtadi, M., Helmke, P., Hebbeln, D., 2012. High interglacial diatom
671 paleoproductivity in the western most Indo-Pacific Warm Pool during the past 130,000
672 years. *Paleoceanography* 27, doi:3210.1029/2012PA002299.
- 673 Sarmiento, J.L., Gruber, N., Brzezinski, M.A., Dunne, J.P., 2004. High-latitude controls of
674 thermocline nutrients and low latitude biological productivity. *Nature* 427, 56–60.
- 675 Shannon, L.V., 1985. The Benguela Ecosystem. 1. Evolution of the Benguela, physical
676 features and processes. In: Barnes, M. (Ed.), *Oceanography and Marine Biology, An*
677 *annual review* 23. University Press, Aberdeen, U.K. pp. 105–182.
- 678 Shannon, L.V., Nelson, G., 1996. The Benguela: Large Scale Features and Processes and
679 System Variability. In: Wefer, G., Berger, W.H., Siedler, G., Webb, D.J. (Eds), *The South*
680 *Atlantic: Present and Past Circulation*. Springer Verlag, Berlin Heidelberg, Germany. pp.
681 163–210.
- 682 Shillington, F.A., 1998. In: Robinson, A.R., Brink, K.H. (Eds.), *The Benguela Upwelling*
683 *System off Southwestern Africa*. *The Sea* 11. pp. 583–604.
- 684 Siddall, M., Rohling, E.J., Thompson, W.G., Waelbroeck, C., 2008. Marine isotope stage 3
685 sea level fluctuations: Data synthesis and new outlook. *Reviews of Geophysics* 46,
686 RG4003, doi:10.1029/2007RG000226.
- 687 Sijp, W., England, M.H., 2008. The effect of a northward shift in the southern hemisphere
688 westerlies on the global ocean. *Progress in Oceanography* 79, 1–19.
- 689 Simon, M.H., Arthur, K.L., Hall, I.R., Peeters, F.J.C., Loveday, B.R., Barker, S., Ziegler, M.,
690 Zahn, R. 2013. Millennial-scale Agulhas Current variability and its implications for salt-

691 leakage through the Indian–Atlantic Ocean Gateway. *Earth and Planetary Science Letters*
 692 383, 101-112.

693 Sundström, B.G., 1986. The marine diatom genus *Rhizosolenia*. Lund University, Lund,
 694 Sweden. Ph.D. Thesis, pp. 1–117.

695 Villanueva, J., Grimalt, J.O., 1997. Gas chromatographic tuning of the U_{37}^K
 696 paleothermometer. *Analytical Chemistry* 69, 3329– 3332.

697 Waelbroeck, C., Labeyrie, L., Michel, E., Duplessy, J.C., McManus, J.F., Lambeck, K.,
 698 Balbon, E., Labracherie, M., 2002. Sea-level and deep water temperature changes derived
 699 from benthic foraminifera isotopic records. *Quaternary Science Reviews* 21, 295-305.

700

701 Figure Captions

702 Figure 1. Location of the study site MD96-2098 and comparison site GeoB3606-1 (white
 703 stars) in the Benguela Upwelling System. Location of core MD96-2087 is shown for
 704 comparison. Seasonally averaged concentration of chlorophyll *a* (mg m^{-3}) for (a) January-
 705 March (austral summer), (b) April-June (austral fall), (c) July-September (austral winter),
 706 and (d) October-December (austral spring) from the years 1998-2009 in 9 by 9 km
 707 resolution (Goddard Space Flight Center, <http://oceancolor.gsfc.nasa.gov/SeaWiFS/>).

708 Figure 2. Site MD96-2098: (a) Stratigraphy: five tie-points (red inverted triangles) based on
 709 oxygen isotope analyses of the benthic foraminifera *Cibicidoides wuellerstorfi* (Pichevin et
 710 al., 2005a, b; revised here) and its correlation with to the *Globigerina inflata* $\delta^{18}\text{O}$ record
 711 from core GeoB1711-4 (12.37°S, 23.32°E, Kirst et al., 1999; Romero, 2010). (b) Total
 712 sedimentation rate ($\text{cm}^{-2} \text{kyr}^{-1}$, black line) for the past 70 kyr (upper 1050 cm of core
 713 MD96-2098).

714 Figure 3. Accumulation rates (AR) of (a) total diatoms (valves $\text{cm}^{-2} \text{kyr}^{-1}$), and concentration
 715 of (b) calcium carbonate (CaCO_3 , %), (c) opal (wt.%), (d) total organic carbon (TOC,

716 wt.%) in cores MD96-2098 (red line) and GeoB3606-1 (grey line), (e) oxygen isotopes
 717 ratios (‰ VPDB) measured on the benthic foraminifera *Cibicidoides wuellerstorfi* (site
 718 MD96-2098), and (f) alkenone-derived SST (°C) off Lüderitz in the Benguela Upwelling
 719 System. Marine isotopic stages (MIS) boundaries are defined after LR04-Stack (Lisiecki
 720 and Raymo, 2007). Glacial stages 2 and 4 are indicated by the grey shadings (upper panel).
 721 The light-blue shading indicates the occurrence of the Last Glacial Maximum (LGM).
 722 Lower panel: the inverted red triangles represent the tie-points for MD96-2098 stratigraphy
 723 (Pichevin et al., 2005a, b), and the inverted dark grey triangles ¹⁴C datings of GeoB3606-1
 724 (Romero, 2010).

725 Figure 4. Cumulative percentage (%) of four diatom groups (see 3.3.2.) in cores MD96-2098
 726 (a; upper panel) and GeoB3606-1 (b; lower panel) off Lüderitz in the Benguela Upwelling
 727 System. References: upwelling (green), pelagic-oligotrophic (light yellow), benthic
 728 (brown), and light grey (coastal planktonic). Marine isotopic stages (MIS) boundaries are
 729 defined after LR04-Stack (Lisiecki and Raymo, 2007). Glacial stages 2 and 4 are indicated
 730 by the grey shadings (upper panel). The light-blue shading indicates the occurrence of the
 731 Last Glacial Maximum (LGM). The black arrow around 17 kyr defines the abrupt shift in
 732 the species composition of the diatom assemblage.

733 Figure 5. Schematic representation of the four phases of changes of atmospheric and
 734 hydrographic features, sea-level stand and nutrient availability off Lüderitz during the past
 735 70 kyr (left panel): (1) 70 kyr - 44 kyr; (2) 44 kyr – 31 kyr; (3) 31 kyr – 19 kyr; and (4) 19
 736 kyr – 6 kyr. Right upper panel: large white star (site MD96-2098), small white star
 737 (GeoB3606-1), blue arrow (Si input), light grey arrow (Southern Hemisphere westerlies),
 738 black/grey arrows (sea level stand), and yellow arrow (trade winds). Different arrow
 739 thickness, and length and color darkness represent the strength of the mechanism discussed
 740 (larger/wider/darker=stronger, smaller/thinner/lighter=weaker). The areal cover of the

741 Lüderitz filament is represented by the color-graded shading streaming offshore from the
742 coastline (darker green tones represent higher productivity/more intense upwelling).

743 Figure 6. Comparison of MD96-2098 and GeoB606-1 data with Agulhas Leakage, wind
744 strength and global sea-level stand. (a) Agulhas leakage (represented by planktonic
745 foraminifera fauna from two cores in the Agulhas Basin, Peeters et al., 2004); (b) variability
746 of sea level (m) (low resolution data, Waelbroeck et al., 2002; high resolution data,
747 Rohling et al., 2009), (c) mean grain size (μm^{-2} , MD96-2087, Pichevin et al., 2005b), (d)
748 SST ($^{\circ}\text{C}$; MD96-2087, blue line, Pichevin et al., 2005b), (e) SST ($^{\circ}\text{C}$; MD96-2098, red
749 line, and GeoB3606-1, black line, this study), (f) total diatom_{AR} (valves $\text{cm}^{-2} \text{kyr}^{-1}$,
750 GeoB3606-1, black line; Romero, 2010), and (g) total diatom_{AR} (valves $\text{cm}^{-2} \text{kyr}^{-1}$, MD96-
751 2098, red line, this study). Black, single headed arrows A and B in (b) mark two-step rapid
752 decreases of sea level stand. Light brown lines represent negatively correlated episodes of
753 (e) SST GeoB3606-1 and (f) total diatom_{AR} GeoB3606-1. Marine isotopic stages (MIS)
754 boundaries are defined after LR04-Stack (Lisiecki and Raymo, 2007). Glacial stages 2 and
755 4 are indicated by the grey shadings (upper panel). The light-blue shading indicates the
756 occurrence of the Last Glacial Maximum (LGM). Ph4 through Ph1 indicate the four phases
757 of westward/eastward migration of the filament front off Lüderitz for the past 70 kyr (see
758 also Fig. 5).

Figure 1
Romero et al.

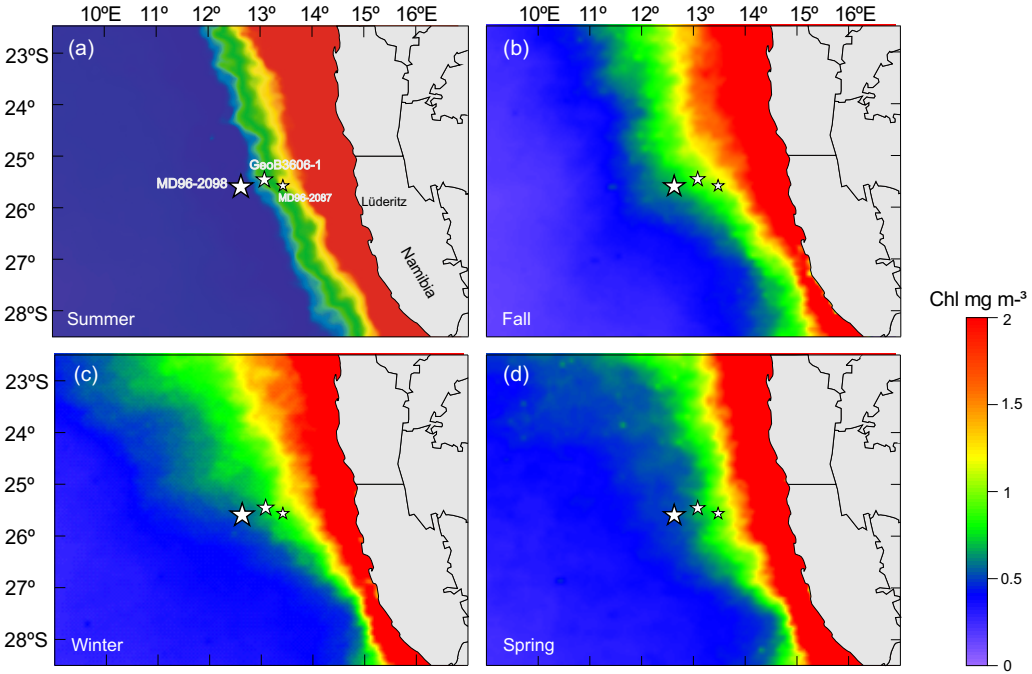


Figure 2
Romero et al.

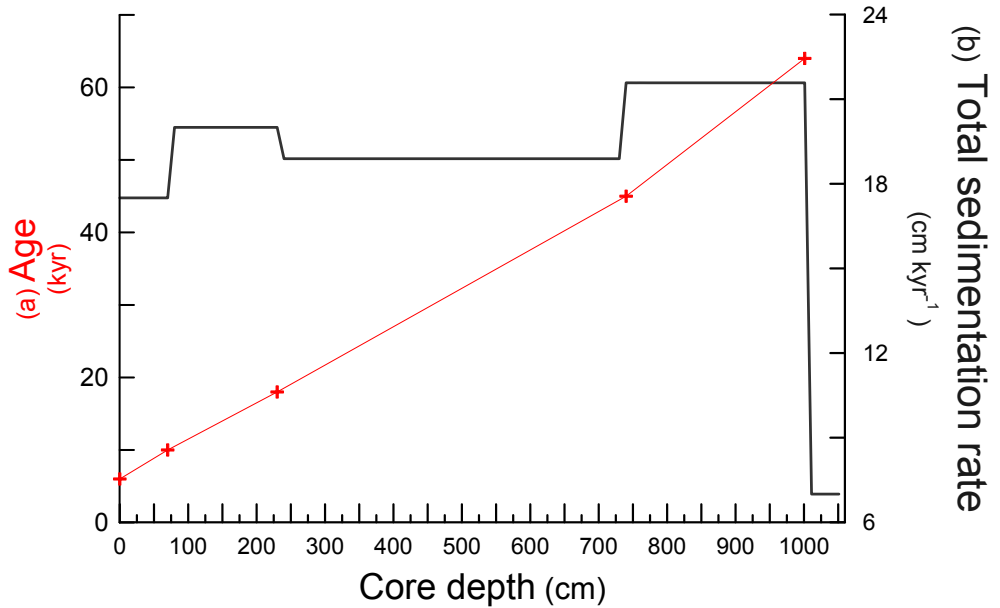


Figure 3
Romero et al.

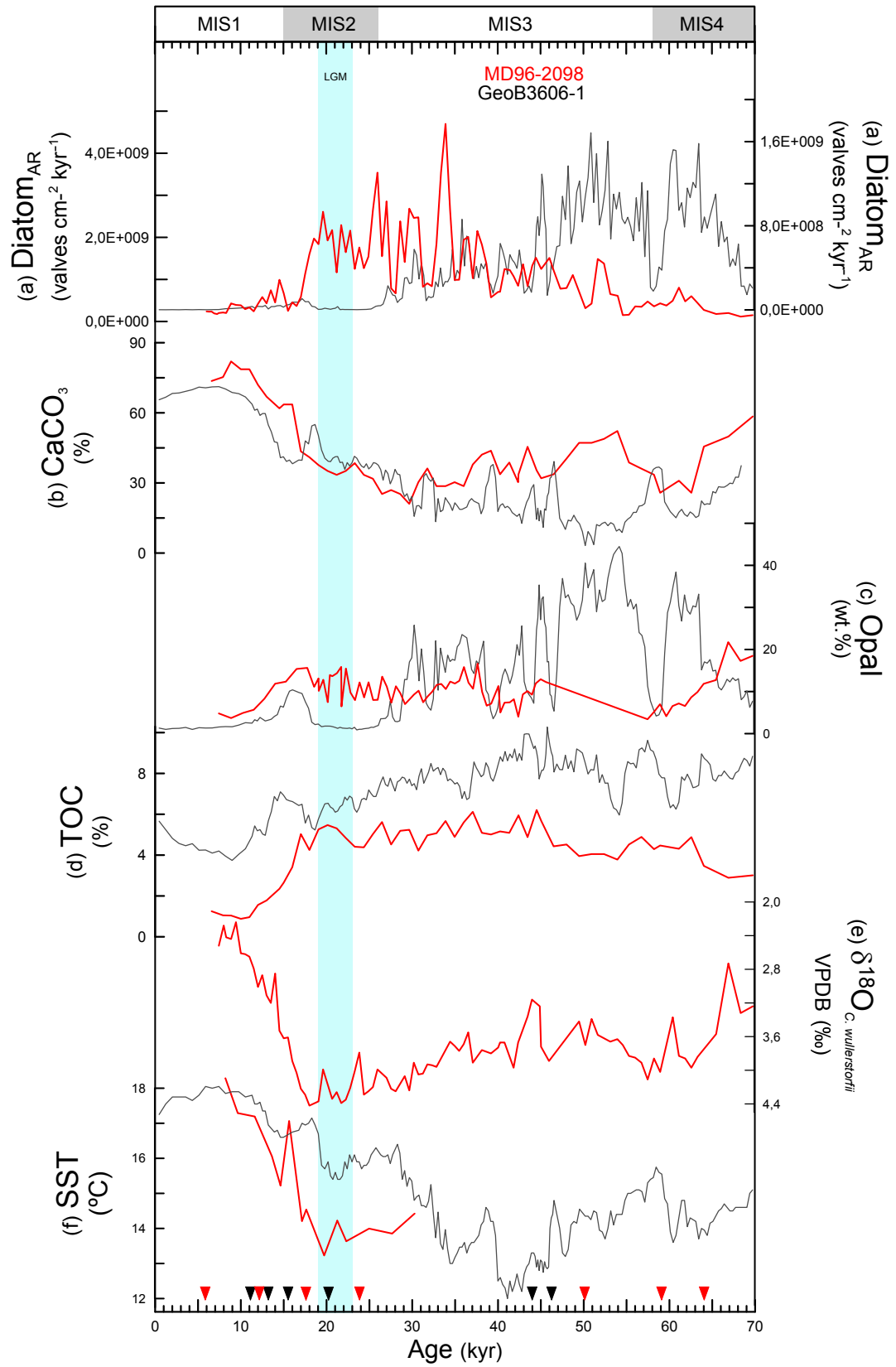


Figure 4
Romero et al.

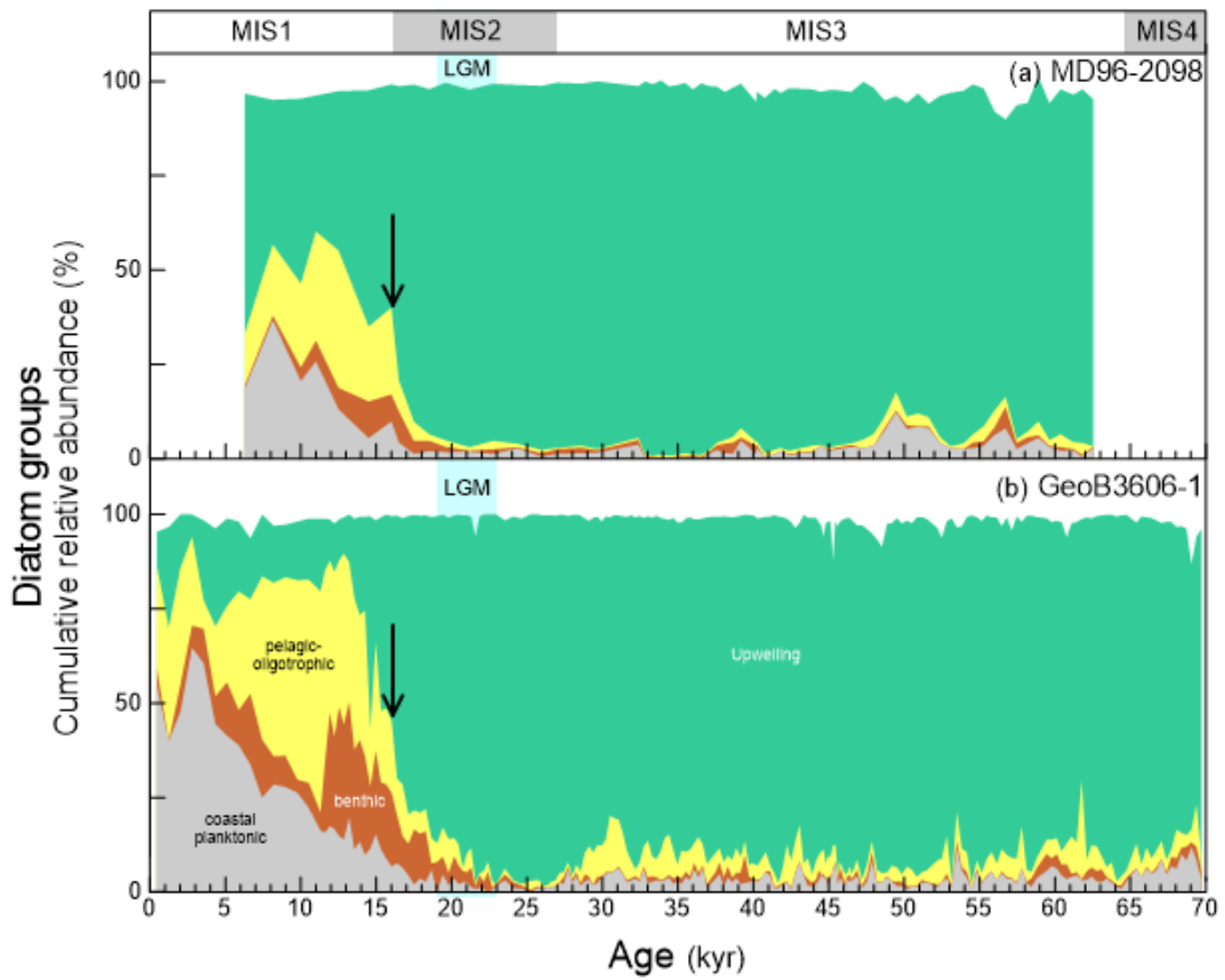
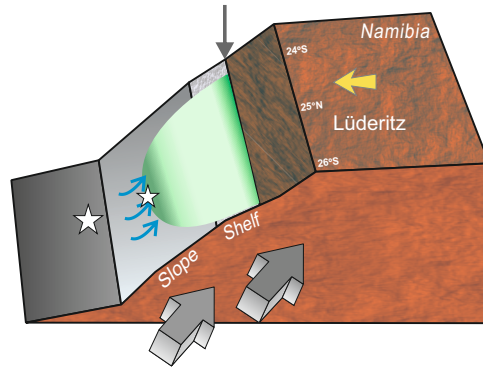


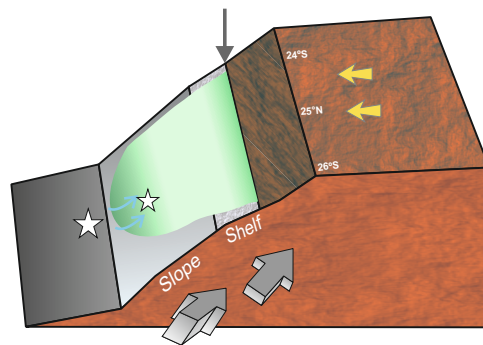
Figure 5
Romero et al.

Phase 1: Late MIS4 to mid MIS3 (70-44 kyr)

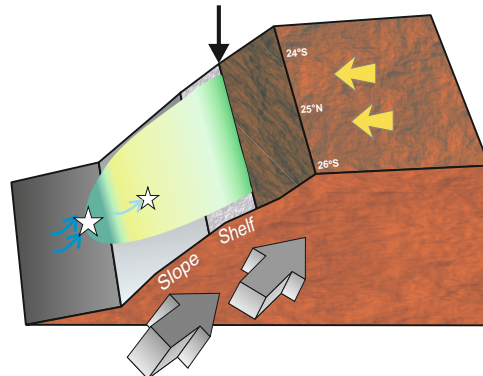


- ☆ MD96-2098
- ☆ GeoB3606-1
- ↗ Si input
- ↙ Southern Hemisphere Westerlies
- ↕ Low / Rise sea-level stand
- ↖ Trade winds

Phase 2: Mid to late MIS3 (44-31 kyr)



Phase 3: Late MIS 3 to LGM (31-19 kyr)



Phase 4: Late deglaciation to mid Holocene (19-6 kyr)

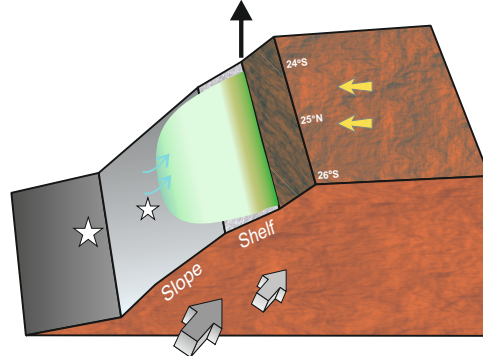


Figure 6
Romero et al.

